crystals

MDPI

Article

Ni-Co Alloy and Multisegmented Ni/Co Nanowire Arrays Modulated in Composition: Structural Characterization and Magnetic Properties

Miguel Méndez [1], Silvia González [1], Víctor Vega [2], Jose M. Teixeira [1], Blanca Hernando [1], Carlos Luna [3] and Víctor M. Prida [1,*]

1 Departamento de Física, Facultad Ciencias, Universidad de Oviedo, Calvo Sotelo s/n, 33007 Oviedo, Asturias, Spain; miguel.mendez82@gmail.com (M.M.); gonzalezgana@uniovi.es (S.G.); mesquitajose@uniovi.es (J.M.T.); grande@uniovi.es (B.H.)

2 Laboratorio de Membranas Nanoporosas, Servicios Científico-Técnicos, Universidad de Oviedo, Campus El Cristo s/n, 33006 Oviedo, Asturias, Spain; vegavictor@uniovi.es

3 Centro de Investigación en Ciencias Físico Matemáticas, Universidad Autónoma de Nuevo León (UANL), Av. Universidad S/N, San Nicolás de los Garza, 66455 Nuevo León, Mexico; carlos.lunacd@uanl.edu.mx

* Correspondence: vmpp@uniovi.es; Tel.: +34-985-103-294

Academic Editor: Arkady Zhukov
Received: 12 January 2017; Accepted: 22 February 2017; Published: 26 February 2017

Abstract: Design of novel multisegmented magnetic nanowires can pave the way for the next generation of data storage media and logical devices, magnonic crystals, or in magneto-plasmonics, among other energy conversion, recovery, and storage technological applications. In this work, we present a detailed study on the synthesis, morphology, structural, and magnetic properties of Ni, Co, and Ni-Co alloy and multisegmented Ni/Co nanowires modulated in composition, which were grown by template-assisted electrodeposition employing nanoporous anodic aluminum oxide as patterned templates. X-ray diffraction, and scanning and high-resolution transmission electron microscopies allowed for the structural, morphological, and compositional investigations of a few micrometers long and approximately 40 nm in diameter of pure Ni and Co single elements, together with multisegmented Ni/Co and alloyed Ni-Co nanowires. The vibrating sample magnetometry technique enabled us to extract the main characteristic magnetic parameters for these samples, thereby evaluating their different anisotropic magnetic behaviors and discuss them based on their morphological and structural features. These novel functional magnetic nanomaterials can serve as potential candidates for multibit magnetic systems in ultra-high-density magnetic data storage applications.

Keywords: nanoporous alumina template; electrodeposition; crystalline structure; magnetic anisotropy; nanowire

1. Introduction

Metallic or metal oxide nanowires (NWs) and nanotubes are 1D nanomaterials that have attracted great attention among the scientific community during previous decades because of their unique features and peculiar physicochemical properties, which have become appealing for a wide range of technological applications, including nanoelectronics [1–3], magneto-optoelectronics [4,5], semiconducting plasmonics, and magneto-plasmonics [6–8], and soft wearable electronic systems [9], among many others. This kind of 1D nanomaterial offers particular advantages due to its intrinsic high aspect ratio, peculiar microstructural characteristics, together with outstanding mechanical, electrical, magnetic, and optical properties, which enable their integration in novel energy conversion devices and data storage media, future stretchable electronic systems, sensors, and micro-nanodevices [10–12].

Nowadays, there are two principal emerging strategies for the synthesis of 1D nanomaterials, mainly based on free-templated [13,14] or template-assisted methods [15]. Among the solid template-based growth methods, the template-assisted electrochemical deposition of single metals and their alloys is one of the most efficient and versatile growing technique popularly employed for the synthesis of 1D nanomaterials embedded inside the pores of polymeric or anodic aluminum oxide (AAO) membranes [16–19]. The synthesis of nanomaterials through the template-assisted electrodeposition method by employing nanoporous alumina membranes (NAMs) as patterned templates, is a commonly used technique for the growing of metallic and magnetic nanostructures inside the pores of anodic alumina with a wire shape geometry and in the nanometer scale range (typically between 20 to 200 nm in diameter size) [20,21]. In comparison with track-etched polycarbonate membranes, which usually exhibit crossed nanopores, the anodic alumina templates provide hexagonal close-packed arrangement of parallel aligned nanopores in a honeycomb spatial structure having a well-defined cylindrical shape, in which can be embedded the electrochemically-grown magnetic NWs by replicating the same dimensions than the former pore sizes.

Most recently, an upgrade of this synthesis method consists in the fabrication of multisegmented nanowires embedded into the pores of these NAMs by changing the sample composition from one layer to the other [22–24], or by varying the diameter size of each nanowire segment [25–29]. These synthesis methods are novel strategies of rising interest for the development of nanomaterials with fine-tuned magnetic anisotropy in a controlled way [30], which plays a pivotal role in determining the magnetic properties and, therefore, allowing for the ability of tailoring the relative orientation of magnetization between each magnetic segment, in order for these multicomponent nanowires to trigger new applications, as in multibit magnetic recording media [31,32].

The controlled design of multisegmented NWs by assembling several layers having different alloy compositions, followed in the former case, is usually achieved by employing two different experimental approaches, the first being through a sequential electrodeposition process, where the composition of each segment is varied by changing the working electrode between different electrolytes; while the second one consists of tuning the composition of each segment by properly swapping the electrodeposition potential or current density, but using a single electrolytic bath [22,33,34]. The first method allows for minimizing the co-deposition phenomenon that is present when different metallic ions can be electrodeposited at similar values of the deposition potential within each segment at the same time. Therefore, a purer chemical composition in each segment of the NW can be achieved in this way [31,35,36]. This synthesis procedure of subsequent segmented magnetic NWs can also lead to poor adhesion between layers with different chemical compositions, or uneven morphological growth, due to changes in the crystalline structure of the respective segments [37] but, at the same time, the assembling building blocks of consecutive segments of the NW having different material composition with a well-defined interface layer at the junctions, which can act as a pinning center for the magnetic domain wall's displacement along the wire length. This fact allows for the magnetization confinement in each NW segment and gives rise to NW arrays with a magnetic multi-domain structure [29,31,35].

In this work we report on a detailed comparative study about the synthesis, microstructure, and magnetic properties of hexagonally-ordered arrangements of soft and hard ferromagnetic NWs made of pure Ni and Co single elements, respectively, together with Ni-Co alloy and multisegmented soft-ferromagnetic and hard-ferromagnetic Ni/Co NWs arrays that were electrochemical grown by template-assisted deposition inside the cylindrical pores of NAMs from two different electrolytes. The observed structural properties were studied and characterized by X-ray diffraction (XRD) and high-resolution transmission electron microscopy (HR-TEM) techniques. The composition of both, multisegmented NWs in the arrangement and isolated NWs after releasing them by chemical etching from the alumina template, were obtained by EDX with SEM and TEM, respectively. The main magnetic properties for all of the synthesized samples were determined from the measurements of their corresponding hysteresis loops carried out by vibrating sample magnetometry (VSM). The magnetic behavior of each sample was correlated with the magnetic anisotropy coming from the

different crystallographic features exhibited by the Ni and Co segments of the NW, together with the additional influence of inter-nanowires magnetostatic interaction among the NWs in the array and the intra-nanowires' dipolar interaction between each segment of the multisegmented NWs, respectively. The obtained results demonstrate that the effective magnetic anisotropy developed in multisegmented Ni/Co NWs is a direct superposition from their Ni and Co former segments, but rather different from the more complex magnetic behavior resulting from the $Ni_{50}Co_{50}$ alloyed NWs. These peculiar multisegmented nanowire arrangements that consist of layered materials with different chemical compositions provide to these novel nanoarchitectures with new on-board multifunctional applications.

2. Experimental Details

2.1. Synthesis of Nanoporous Anodic Alumina Membranes

The starting AAO templates were prepared under mild-anodization conditions by following a two-step anodization process [38,39] in oxalic acid electrolytes. The starting high purity Al foils (99.999%, Goodfellow, Huntingdon, England), were first previously cleaned by sonication in isopropanol and ethanol, and subsequently electropolished to smooth the surface in a vigorously stirred mixture of perchloric and ethanol (1:3 vol.) for 5 min at 5 °C and at the applied voltage of 20 V. After following this sequential pre-treatment until reaching a mirrored polishing, the substrates were cleaned with distilled water (18.2 MΩ/cm). The first anodization process was performed in 0.3 M oxalic acid aqueous electrolyte, vigorously stirred in order to ensure the concentration and temperature homogeneity of the bulk electrolyte, at certain temperature ranging between 1–3 °C. The value of the anodization voltage applied between the sample and the Pt counter electrode, was kept constant at 40 V during 24 h. After the first anodization step, the porous alumina layer was removed by wet chemical etching in a mixture of phosphoric and chromic acids at 35 °C for 8 h.

The second anodization step was performed under the same conditions and with the same operation times (24 h), in order to adjust the final thickness of AAO to around 43.2 μm. This step results in the growth of a highly-ordered NAM on top of the starting Al substrate. Afterwards, each of the NAM templates were immersed in 5 wt% phosphoric acid at 30 °C to widen the diameter of the pores. The corresponding operation time was 15 min. The remaining Al substrate was partially removed under chemical etching in an aqueous mixture of HCl and $CuCl_2$, by exposing an area of around 1 cm^2 of the NAM template's backside. The alumina barrier layer at the bottom of the pores was removed by exposing it to 5 wt% H_3PO_4 at room temperature for 2 h, thus resulting in a two-side opened NAM, as schematically shown in Figure 1a.

2.2. Surface Functionalization by Atomic Layer Deposition, Au Sputtering and Electrodeposition

The so-obtained NAM templates were further modified by conformal coating their surface and inner pore walls with a thin SiO_2 layer around 4 nm in thickness by means of atomic layer deposition (ALD), as schematically shown in Figure 1b. The SiO_2 coating reduces both the pore diameter and porosity of the AAO, but it also seems to affect the electric fixed charge on the membranes surface [40]. Conformal atomic layer deposition of SiO_2 coating on the AAO samples was performed in an ALD Savannah 100 thermal reactor from Cambridge Nanotech (Ultratech CNT, Whaltham, MA, USA), with high purity Ar as the carrier gas. The precursors employed were 3-aminopropyltriethoxysilane (100 °C, 2 s pulse), water (20 °C, 0.5 s pulse), and ozone (room temperature, 2 s pulse). The substrate temperature during the deposition procedure was fixed to 180 °C. The silica deposition was performed in stop-mode (45 s exposure time, 60 s pump time) to ensure homogeneous coating along the inner channels of the NAM templates [40,41], and the number of deposition cycles was set to 90.

Afterwards, the backside of the NAM templates was gold-coated by means of sputtering and further electrodeposition of a continuous gold layer, which serves as working electrode in the subsequent multisegmented Ni/Co electrodeposition process, as indicated in Figure 1c,d, respectively.

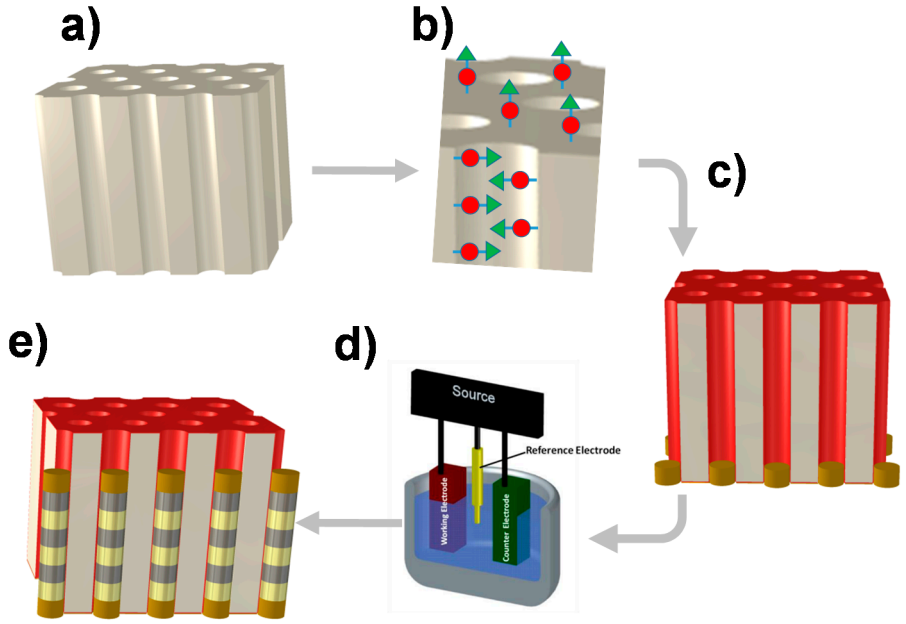

Figure 1. Sketch of the different steps employed for the template-assisted fabrication of segmented nanowire arrays: (**a**) the starting nanoporous AAO template, (**b**) SiO_2 surface functionalization of the NAM by atomic layer deposition (ALD), (**c**) SiO_2 coated NAM template with gold nanocontacts, (**d**) sequential electrodeposition of Ni and Co in a three-electrode setup, and (**e**) multisegmented Ni/Co NWs array embedded inside the SiO_2 coated pores of the NAM template.

2.3. Electrodeposition of Magnetic Nanowires and Their Morphological, Structural, and Magnetic Characterization

The functionalized NAM is then used as a template for the electrochemical growth of single element of Ni or Co nanowires, together with multisegmented Ni/Co and $Ni_{50}Co_{50}$ alloyed (Ni-Co) NWs arrays, as schematically shown in Figure 1e. Nickel and cobalt sulfate and chloride salts were used to produce Watts-type electrolytic solutions that were employed for electrodeposition of metals inside the nanopores of the NAM template [42]. The pH of the electrolytes was adjusted between 4–4.5 with the addition of 1 M NaOH solution and the electrodeposition temperature was fixed to 35 °C. This process was performed employing the potentiostatic mode at −1.2 V in a three-electrode electrochemical cell equipped with an Ag/AgCl reference electrode, an insoluble Pt mesh counter electrode, and the gold-SiO_2 coated NAM template acting as the working electrode displayed in Figure 1c. The duration of the potentiostatic deposition pulses was adjusted to 480 s for the growing of single element Ni NWs, 328 s for the pure Co NWs, 50 s of Ni and 35 s of Co for the multisegmented Ni/Co NWs arrays, and 328 s for the Ni-Co alloyed NWs, therefore resulting in an alloy of $Ni_{50}Co_{50}$, accordingly, with the estimated deposition rate for each metal or alloy, respectively. For the particular case of multisegmented Ni/Co NWs, a two-electrolytic bath electrochemical deposition was carried out, whereupon after the electrodeposition of each single element segment, we rinsed the deposition cell with distilled water and ethanol, and then we dried it before starting a new electrodeposition process for another segment with the second electrolyte.

The morphology, chemical composition, and microstructure of the samples were studied by scanning electron microscopy (SEM, JEOL 6610LV, JEOL Ltd., Tokyo, Japan), energy dispersive X-ray microanalysis (EDX), high-resolution transmission electron microscopy (HRTEM, JEOL JEM-2100, JEOL Ltd., Tokyo, Japan), and X-ray diffraction (XRD), respectively. XRD patterns were collected in a Bragg-Brentano geometry on a PANalytical X'Pert Pro MPD diffractometer (PANalytical B.V. Almelo, The Netherlands) equipped with a "Johansson" Ge(111) primary monochromator (producing strictly monochromatic Cu $K\alpha_1$ radiation) and a PIXcel detector based on Mediapix2 technology. The angular range was selected between 35° to 105°, employing a counting time of 150–450 s depending on sample

composition. The MAUD (Material Analysis Using Diffraction, Luca Lutterotti, Trento, Italy) [43–46], program was used for the fitting of entire XRD curves using the Rietveld method in order to determine the weight ratio of the crystalline phases present in the samples and their lattice parameters.

All magnetic measurements were performed at room temperature (RT) in a vibrating-sample magnetometer (VSM, Versalab-QD, LOT-QuantumDesign GmbH, Darmstadt, Germany), in the magnetic field range between ±3 Tesla (T), applied along both the parallel and perpendicular directions to the NWs longitudinal axis.

3. Results and Discussion

3.1. Morphological and Structural Characterizations by SEM and TEM

The highly-ordered nanopore distribution of the SiO_2-coated anodic alumina membranes, employed as templates for the fabrication of Ni, Co, their Ni-Co equiatomic alloy, and the multisegmented Ni/Co NWs arrays employed in this work, can be observed in the SEM top view image displayed in Figure 2a. The parallel aligned nanopores have a well-defined mean diameter of around 43 ± 4 nm, an interpore distance of about 105 nm, and follow a hexagonal close-packed geometry.

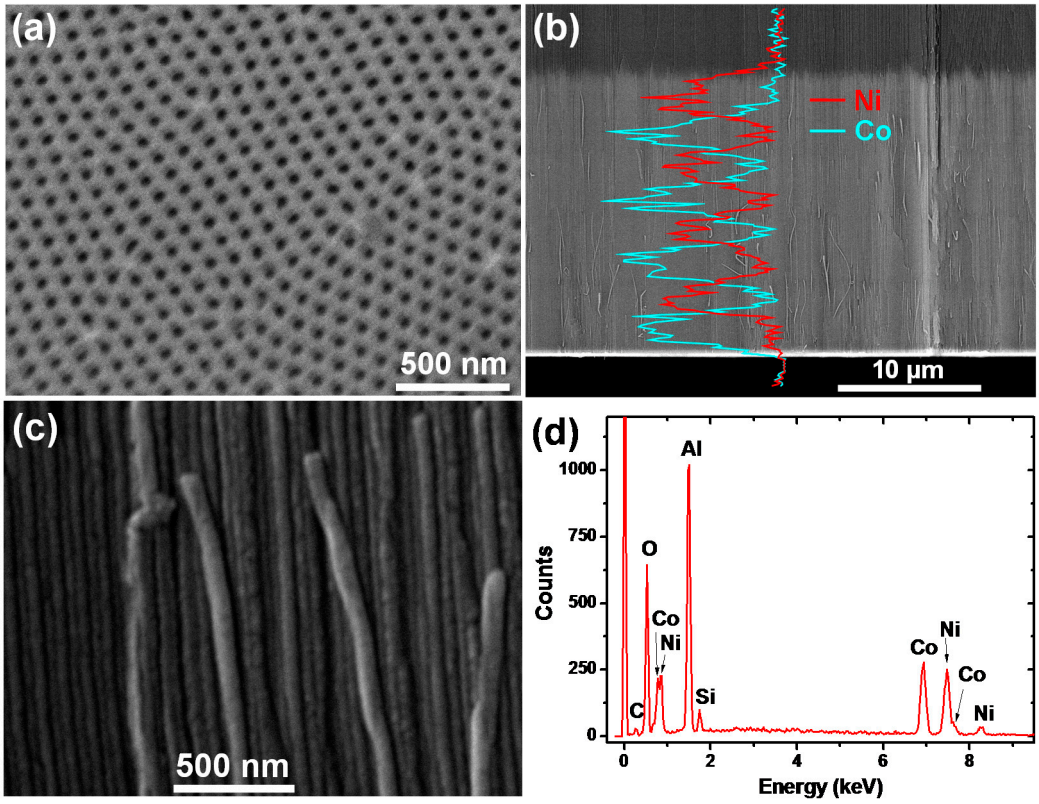

Figure 2. (**a**) SEM top view of a typical NAM employed as template for the fabrication of multisegmented Ni/Co NWs arrays. (**b**) SEM cross-section of multisegmented Ni/Co NWs embedded in the NAM template. The line scans superimposed on the image represent the variation of Co and Ni content along the membrane thickness. (**c**) SEM cross-section image of Ni-Co alloyed NWs that are embedded in a NAM template. (**d**) EDX spectrum recorded from the cross-section image shown in (**c**).

Figure 2b shows the SEM cross-section image of a typical NAM after being electrochemically filled with an alternating sequence of Ni and Co deposits. The sequential deposition process results in the growth of segmented NWs, formed by alternating the Ni and Co segments of roughly 2–2.5 µm in length, giving rise to a nanowire total length of around 18.6 µm, corresponding to eight segments with different chemical composition. The modulation in the composition of each segment can be clearly

observed in the EDX line scans superimposed in Figure 2b, which indicate the periodically fluctuating amount of Ni and Co corresponding to each segment of the multisegmented Ni/Co magnetic NWs array. Figure 2c shows a SEM cross section image of Ni-Co alloyed NWs with around 40 nm in diameter that are embedded in the pores of the NAM template, while Figure 2d shows the corresponding EDX spectrum obtained from the region shown in Figure 2c, and that reveals an approximate composition of $Ni_{50}Co_{50}$.

In order to obtain more information about the microstructure of the segmented Ni/Co NWs, they were studied by HR-TEM, after selective chemical dissolution of the nanoporous alumina template as described in detail elsewhere [42,47]. Figure 3a shows a low magnification STEM image, whereas Figure 3b shows the EDX elemental map of chemical composition distribution of the same NWs area carried out under high angle annular dark field-scanning transmission electron microscopy (HAADF-STEM) mode.

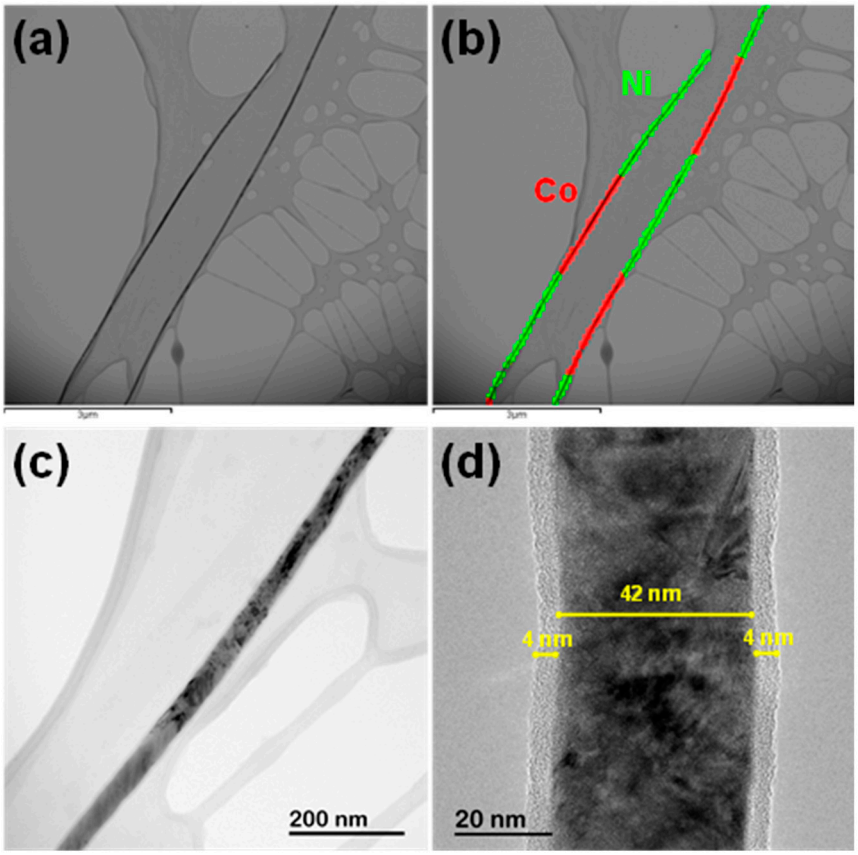

Figure 3. (**a**) HR-TEM characterization of multisegmented Ni/Co NWs after releasing them from the NAM template. (**b**) Low-magnification STEM image of multisegmented Ni/Co NWs and corresponding EDX element distribution map. The bar scales of these two upper figures represent 3 microns, respectively. (**c**,**d**) High-magnification HR-TEM images of segmented Ni/Co isolated NWs.

The elemental composition mappings of the Ni/Co NWs, confirmed their multisegmented structure with alternating segments of metallic nickel and cobalt, respectively. The Ni segments have a length of approximately 2.5 μm, while the Co ones are slightly shorter, having around of 2 μm in length. Figure 3c,d display higher magnification HR-TEM images, showing that the Ni/Co NWs are rather homogeneous in diameter despite their multisegmented structure, displaying a metallic core with diameters of around 42 nm, in good agreement with the expected value obtained from pore diameter measurements performed by SEM in the top view of the anodic alumina template shown

in Figure 2a. The inner metallic core is surrounded by an amorphous, electron transparent region of around 4 nm in thickness that corresponds to the SiO_2 shell.

Figure 4 presents two selected area electron diffraction (SAED) polycrystalline-like patterns (Figure 4b,d) of two different segments of a Ni/Co NW, as shown in Figure 4a,b. The studied segment of Figure 4a presents a SAED pattern with diffraction spots that can be associated with the face-centered cubic structure of metallic nickel (JCPDS 4-850). On the other hand, the segment analyzed in Figure 4b displays a SAED pattern that can be indexed to hexagonal close-packed cobalt (JCPDS 5-727). However, some observed spots could be also ascribed to a nickel (JCPDS 4-850) or cobalt phase (JCPDS 15-806).

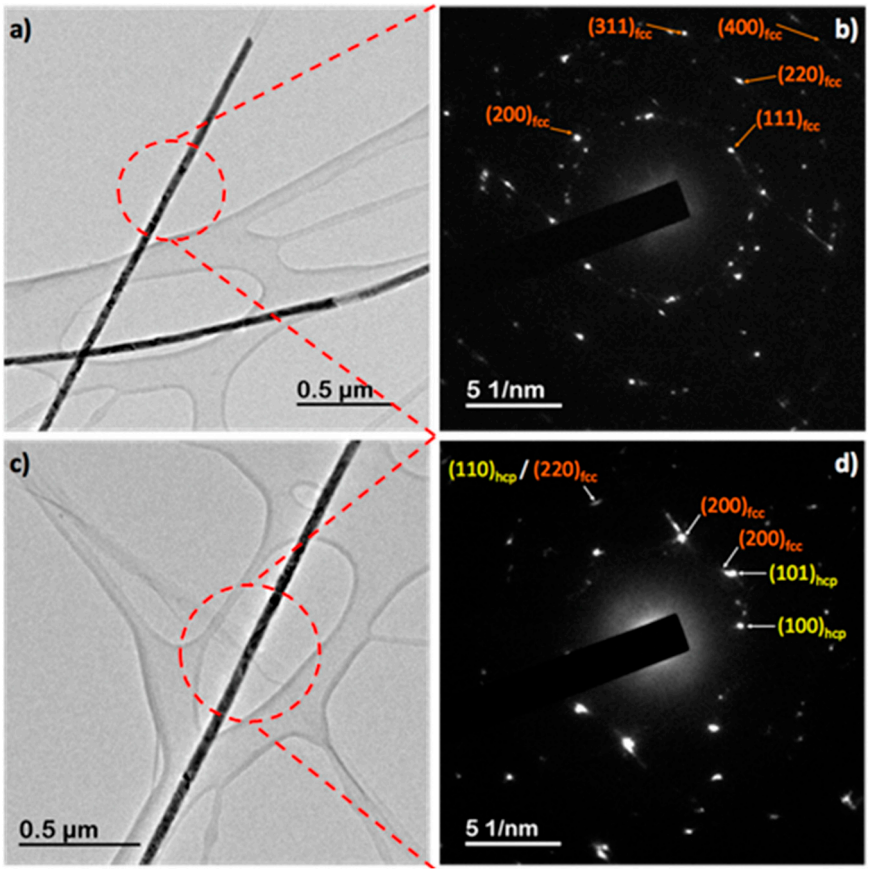

Figure 4. (**a**,**c**) show the selected TEM images of two isolated ferromagnetic NWs made of subsequent Co and Ni segments. (**b**,**d**) display the SAED analysis of the nanowire regions indicated in (**a**,**c**), corresponding to Ni and Co segments, respectively.

3.2. XRD Analysis

Figure 5a depicts the XRD pattern of the pure Co NWs. The diffraction peaks observed at 2θ values of 41.66°, 44.43°, 47.40°, 75.86°, 84.12°, 90.55°, 92.40°, and 94.43° can be indexed to (100), (002), (101), (110), (103), (200), (112), and (201) crystallographic planes of the hexagonal close-packed (hcp) cobalt phase (JCPDS 05-0727), respectively. The obtained lattice parameters were a = 2.4999 ± 0.0001Å and c = 4.0791 ± 0.0009 Å, which are very close values to the bulk ones (a = 2.505 ± 0.0002Å and c = 4.060 ± 0.0002 Å, JCPDS 05-0727). Interestingly, the relative intensity of several of these peaks was dramatically different than the expected ones for a polycrystalline sample (Figure 1a). For instance, the (100) peak is the most intense peak whereas the (101) reflection appears as a very inhibited peak. These results suggest that the cobalt NWs exhibit a growth texture in the <100> direction and a clear inhibition in the <101> growth direction, probably due to the favoring growth of determined crystal directions under the control of the confined growth into the pores of the alumina membrane template.

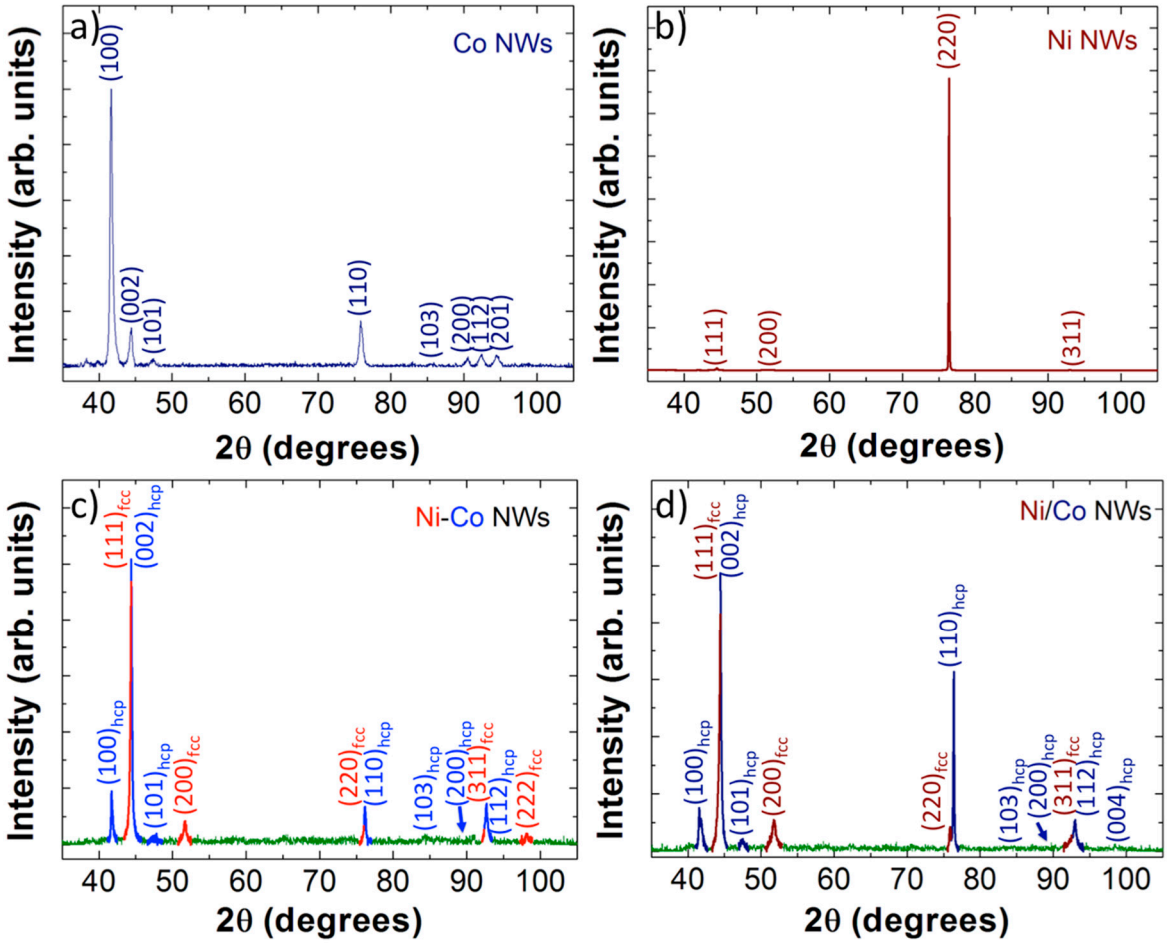

Figure 5. XRD patterns corresponding to the samples: (**a**) Co NWs, (**b**) Ni NWs, (**c**) Ni-Co alloyed NWs, and (**d**) multisegmented Ni/Co NWs.

The mean coherent lengths, L_{hkl}, estimated from the position and full width at half maximum (FWHM) of these peaks are presented in Table 1. Also, the relative intensities of these peaks and the expected relative intensities according to the JCPDS 05-0727 file are shown in the same table.

Table 1. Mean coherent lengths and relative peak intensities of the diffraction peaks corresponding to the Co phase. Also, the relative intensities according to the JCPDS 05-0727 file have been added for comparison proposes.

Diffraction Peak	L_{hkl} (nm)	Sample Relative Intensity (%)	Bulk Relative Intensity (%)
(100)	25	100	20
(002)	21	14	60
(101)	-	2	100
(110)	21	16	80
(103)	-	-	80
(200)	20	3	20
(112)	17	4	80
(201)	16	4	60
(004)	-	-	20

Figure 5b depicts the XRD pattern of pure Ni NWs. A very intense and sharp diffraction peak is observed at 76.50°. Moreover, three very weak peaks are also observed at 44.50°, 51.85°, and

98.43°, respectively. These peaks are associated to the (220), (111), (200), and (222) planes of the fcc nickel phase (JCPDS 04-0850), respectively, and the estimated value of the lattice parameter was a = 3.525 ± 0.001 Å. From this diffraction pattern, it is clearly revealed that this sample exhibits a strong crystalline preference to <110> texture. In fact, the mean coherent lengths perpendicular to this direction, L_{220} = 116 nm, was around one or two orders of magnitude higher than the others (L_{111} = 29 nm, L_{200} = 6 nm and L_{311} = 16 nm), confirming the tendency to grow along the <110> direction. The corresponding mean coherent lengths and peak intensities estimated from the diffraction patterns for Ni crystal phase, are presented in Table 2.

Table 2. Mean coherent lengths and relative peak intensities of the diffraction peaks corresponding to the Ni phase. Additionally, the expected relative intensities according to the bulk fcc for Ni (JCPDS 04-0850) have been added for comparison purposes.

Diffraction Peak	L_{hkl} (nm)	Sample Relative Intensity (%)	Bulk Relative Intensity (%)
(111)	29	~1	100
(200)	6	~1	42
(220)	116	100	21
(311)	16	<1	20
(222)	-	-	7

Figure 5c presents the XRD pattern corresponding to the sample of Ni-Co alloyed nanowires. In this pattern, the diffraction peaks corresponding to both, the hcp and fcc phases of Ni-Co NWs are observed. Data about the mean coherent lengths and relative peak intensities extracted from them are collected in Table 3. The calculated lattice parameters were a = 3.5358 ± 0.0005 Å, for the fcc phase, and a = 2.4966 ± 0.0004 Å and c = 4.077 ± 0.0003 Å for the hcp phase. The estimated weight ratios of the two crystalline phases were 95.6% ± 0.2% and 4.4% ± 0.6% for the fcc and hcp phases, respectively. It is important to note that the growth in the <101> direction of the hcp crystal phase is inhibited in a similar way than in pure Co NWs. On the other hand, the sharp peak at 44.33° indicates a preference to growth in the fcc <111> and/or in the hcp <002> directions.

Table 3. Mean coherent lengths and relative peak intensities of the diffraction peaks corresponding to the Ni and Co phases for the Ni-Co alloyed NWs.

Diffraction Peak	L_{hkl} (nm)	Sample Relative Intensity (%)	Bulk Relative Intensity (%)
$(100)_{hcp}$	36	18	20
$(111)_{fcc}/(002)_{hcp}$	43	100	100/60
$(101)_{hcp}$	-	4	100
$(200)_{fcc}$	20	8	42
$(220)_{fcc}/(110)_{hcp}$	37	13	21/80
$(103)_{hcp}$	-	4	80
$(311)_{fcc}/(112)_{hcp}$	30	14	20/80
$(222)_{fcc}$	-	4	7

Figure 5d presents the XRD pattern of the array with multisegmented Ni/Co NWs. This pattern confirms the presence of two crystalline phases whose diffraction peaks can be indexed to the hcp cobalt phase (JCPDS 05-0727) and the fcc nickel phase (JCPDS 04-0850), with the lattice parameters a = 3.529 ± 0.0001 Å for fcc, and a = 2.4966 ± 0.0004 Å and c = 4.077 ± 0.0003 Å for hcp phases, and having weight ratios of 80.9% ± 0.6% and 19.1% ± 0.6%, respectively. Table 4 collects the data of mean coherent lengths and relative peak intensities of the diffraction peaks corresponding to the Ni and Co crystal phases of this sample.

Table 4. Mean coherent lengths and relative peak intensities of the diffraction peaks corresponding to the Ni and Co phases for the multisegmented Ni/Co NWs.

Diffraction Peak	L_{hkl} (nm)	Sample Relative Intensity (%)	Bulk Relative Intensity (%)
$(100)_{hcp}$	20	15	20
$(111)_{fcc}/(002)_{hcp}$	42	100	100/60
$(101)_{hcp}$	15	4	100
$(200)_{fcc}$	15	9	42
$(110)_{hcp}$	81		80
$(103)_{hcp}$	-	-	80
$(311)_{fcc}$	-	9	20
$(112)_{hcp}$	-	64	80
$(222)_{fcc}$	-	4	7

3.3. Magnetic Properties

The room temperature hysteresis loops collected for all samples are shown in Figure 6, showing the magnetization versus magnetic field loops applied in parallel and perpendicularly to the NWs longitudinal axis for Ni, Co, multisegmented Ni/Co, and Ni-Co alloy NWs, respectively.

First, focusing only on the single element composition NWs (Ni and Co), the parallel applied magnetic field configuration exhibits a squared hysteresis loop, as predicted for an infinitely long cylinder with strongly defined uniaxial anisotropy [48], with similar coercive fields (*Hc*) and a remanence magnetization ($m_r = Mr/Ms$) of 0.86 and 0.30 for Ni and Co, respectively. Table 5 summarizes the mentioned magnetic parameters of all the studied samples.

In both cases an anisotropic magnetic behavior is present, with a well-defined easy magnetization axis (EA) parallel to the nanowires longitudinal direction, evidencing the dominant role of shape anisotropy. The small tilting of the loops that is more evident for the Co NWs (larger saturation magnetization), is attributed to the inter-nanowire magnetostatic interactions [49–52] and explains the lower value of m_r for Co NWs. In contrast, in the perpendicular configuration one detects narrow hysteresis loops with small H_C and remanence magnetization, as theoretically expected [48].

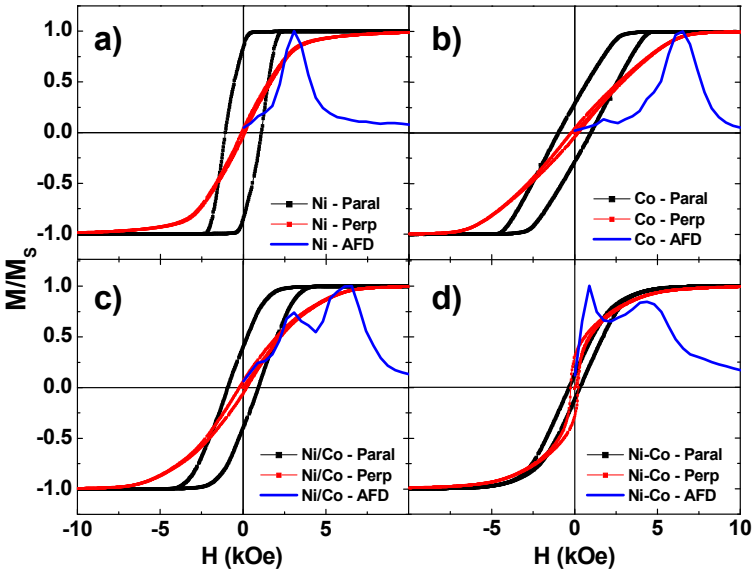

Figure 6. Room temperature magnetic hysteresis curves, *M(H)*, for (**a**) Ni, (**b**) Co, (**c**) multisegmented Ni/Co, and (**d**) Ni-Co alloy NWs, in both parallel and perpendicular directions with respect to the longitudinal axis of the NWs, together with the anisotropy field distribution (AFD) curves calculated according to [53].

Table 5. Magnetic parameters of the NW samples obtained from the room temperature *M(H)* measurements depicted in Figure 6.

H (Oe); m	Ni	Co	Ni/Co	Ni-Co
H_c (//)	1098	971	930	337
H_c (⊥)	103	205	216	231
m_r (//)	0.86	0.30	0.40	0.13
m_r (⊥)	0.04	0.04	0.06	0.29
H_{an}	3064	6532	3076/6348	896/4154

Additional and relevant information can be obtained from the anisotropy field distribution (AFD) curves calculated for each sample and illustrated in Figure 7. The AFD curves have been obtained from the numerical derivative of the descent branch, from positive saturation of the magnetization down to the remanence, of the perpendicular hysteresis loop of NWs arrays, according to [42,47,53,54]. This method provides a simple approach to determine the most prevalent value of the anisotropy field (*Han*) of a magnetic system. Overall, one observes a single AFD curve for Ni and Co NWs and two AFD curves for the NW arrays modulated in composition. The anisotropy field, extracted from the maximum value of the AFD curves, is clearly larger for Co (*Han* ~6532 Oe) than Ni (*Han* ~3064 Oe) array of NWs, (see Table 5). In the case of the NW arrays modulated in composition, one is able to determine two *Han* fields corresponding to the two observed AFD curves. The mutisegmented Ni/Co NW arrays show two *Han* field values (*Han* (Ni) ~3076 Oe; *Han* (Co) ~6348 Oe) that perfectly match with each *Han* field value of the single composed Ni and Co NWs, respectively, indicating that its magnetic behavior can be considered as a superposition of the individual magnetic behaviors of each Ni and Co NWs. This fact can be clearly observed from the AFD curves of all the studied samples, as illustrated in Figure 7. However, the alloyed Ni-Co NW array display one *Han* field value (~896 Oe) that is smaller than the previously mentioned *Han* field values, and another one (~4154 Oe) that is in between them (as indicated in Table 5). Additionally, the *M(H)* behavior becomes less anisotropic with *Hc* (//)~*Hc* (⊥) and m_r (//)~m_r (⊥), resembling the magnetic behavior of spherical nanoparticles, but still with a considerable coercivity.

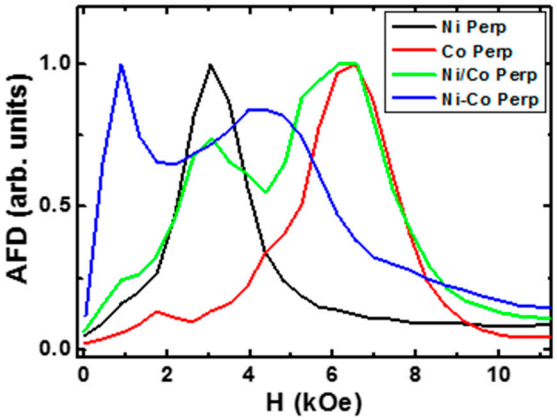

Figure 7. AFD curves calculated from the perpendicular *M(H)* loops of Figure 6 according to [53] for Ni, Co, multisegmented Ni/Co, and Ni-Co alloy NWs, respectively.

In the studied arrays of NWs, the effect of geometrical parameters, like NW diameter, center-to-center distance, and length, over the magnetic properties is the same for all the samples since they did not change significantly from sample to sample. Therefore, only the changes introduced by the modulation in the composition of the NWs should be responsible for the observed differences between their magnetic behaviors. In addition to the intra-wire (i.e., shape anisotropy) and inter-wire magnetostatic effect, contributions to the corresponding magnetic anisotropy, the magnetocrystalline

anisotropy that favors the alignment of the magnetization along preferential crystallographic directions (depending on the symmetry of the crystal and the sign of the constants), can also play a role on the magnetic behavior of the studied systems, despite the polycrystalline nature, although textured, of our samples. The XRD spectra of our samples show extremely intense peaks compared to the patterns of a standard polycrystalline powder (JCPDS sheets). These peaks with enhanced intensities are indicating growth preferences in the material. Since the samples are NWs, this preferential direction (texture) can be associated to the long axis of the NW. The crystal size in this direction is tens of nm and not microns for all of the samples, indicating the polycrystalline nature of the NWs.

For the pure Co NW sample, the peak (100) associated to the hcp phase has a much higher intensity than expected for a polycrystalline powder, illustrating that the <100> direction is the preferred direction of growth that should be parallel to the long axis of the NW. For the Ni sample, the NWs are crystallized in the fcc phase and are strongly textured along the <110> direction, being the preferential direction of growth (long axis). In the multisegmented Ni/Co NWs, we have XRD peaks corresponding to two phases: fcc and hcp. It is observed that the peak around 44° is extremely intense, indicating that the sample is also textured. This peak could correspond to the planes (111) and/or (002) of the Ni fcc and Co hcp phases, respectively. The peak (110) of the hcp phase of Co is also highlighted. It is important to note that, in either case, we have a different texture than in the hcp and fcc phases of the single Co and Ni NWs, respectively, which can be ascribed to the competition between the formation of both crystal phases that can be influenced by epitaxial growth, due to the possible seed layer effect present on a multilayer system. Hence, the growth directions <111>, <001>, and <110> should be along the longitudinal axis of the Ni/Co NWs. The Ni-Co alloyed NWs show a similar texture to the multisegmented Ni/Co ones, but also different from the single Co and Ni NWs, which may be ascribed to a competition between the fcc and hcp crystal phases during the growing process, exhibiting a large peak intensity at around 44° corresponding to the <111> fcc and/or <001> hcp directions. This is the only sample in which *Hc* (//) is not much larger than *Hc* ($\perp$), indicating that the magnetocrystalline anisotropy is competing with the shape anisotropy. For Co, the <001> hcp crystallographic direction coincides with the magnetization EA while the <111> fcc direction corresponds to a hard magnetization axis. In the case of Ni, the <111> fcc direction is the magnetocrystalline axis of the easy magnetization. Therefore, the magnetic behavior of the *M(H)* hysteresis curves suggest that Ni-Co alloy NWs arrays are mainly crystallized in the fcc phase with <111> texture. The effective anisotropy of the single Ni and Co NW arrays are clearly dominated by the shape anisotropy since the <110> fcc and <100> hcp are crystallographic directions of hard magnetization. For the multisegmented Ni/Co NW arrays, we found a preferential <111> fcc (for Ni) and <001> hcp (for Co) crystallographic directions of easy magnetization axis aligned with the longitudinal EA of the NW defined by the shape anisotropy, meaning that both anisotropies contribute to a magnetization EA along the axial direction of the NW.

4. Conclusions

Segmented Ni/Co NWs arrays made of successive alternating layers with pure Ni and Co elements have been synthesized by template-assisted electrodeposition in nanoporous alumina membranes employed as patterned templates. For comparison, pure Ni and Co NWs, together with equally-mixed $Ni_{50}Co_{50}$ alloy NWs were also fabricated by following a similar procedure. The NWs dimensions are, in all cases, around of 45 nm in diameter, 12–18 microns in length and the inter-nanowire distance in the arrangement was about 105 nm, resulting for the particular case of Ni/Co NWs in Ni segments having 2.5 μm in length, but shorter Co segments of 2 μm length. A thin SiO_2 cover layer of a few nanometers has also been previously deposited by ALD inside the pores of the NAMs, in order to protect the NWs from corrosion and give them more mechanical robustness when releasing from the alumina template. The preferential crystalline growth directions are parallel to the NWs axis for all studied samples, being along <100>hcp for Co and <110>fcc for Ni NWs, while there is a strong magnetocrystalline competition between <111>fcc and <001>hcp for the Ni-Co alloy

NWs, and similar behavior can be also observed for the <111>fcc and/or <001>hcp and <110>hcp crystalline phases for the case of multisegmented Ni/Co NWs. From magnetic hysteresis loops it can be observed that the easy magnetization axis of multisegmented Ni/Co NWs lies parallel to the NWs length, indicating the strong role played by the shape anisotropy due to the high aspect ratio exhibited by these samples. The magnetic measurements also allow appreciation of the influence of magnetostatic dipolar interaction from both the inter-wires in the arrangement and the intra-nanowires interaction due to the layered structure of multisegmented Ni/Co NWs. AFD curves calculated for the Ni, Co, and multisegmented Ni/Co NWs arrays allow distinguishing the strong competition between the two magnetic phases, the softer-ferromagnetic characteristic of Ni, and the harder ferromagnetic characteristic for Co, which are present at the same time in the segmented structure displayed by Ni/Co NWs arrays, which determines the global magnetic behavior of this sample. These peculiar multisegmented NWs arrangements formed by layered materials with different chemical compositions, render to these novel nanoarchitectures with new on-board multifunctional applications, as in multibit systems for ultra-high-density magnetic data storage media.

Acknowledgments: This work has been financially supported by the Spanish Ministry of Economy and Competitiveness (MINECO) under research projects N[a] MAT2013-48054-C2-2-R and MAT2016-76824-C3-3-R, together the Principality of Asturias from FICyT project No. FC-15-GRUPIN14-085. The authors thank also to A. Hidalgo for helping with sample fabrication and the technical support provided by Common Scientific-Technical Services of Research from University of Oviedo SCTs.

Author Contributions: V. M. Prida and B. Hernando conceived and designed the concept of the work and led the research projects. M. Mendez and V. Vega synthesized the samples. S. García and V. Vega performed the morphological and compositional analysis together with the microstructural characterization of magnetic nanowires by SEM and TEM. C. Luna carried out the structural analysis of samples by XRD and HR-TEM. J. M. Teixeira carried out the magnetic characterization of nanowires by measuring the hysteresis loops. M. Mendez, V. Vega, S. Garcia, J. M. Teixeira, C. Luna, and V. M Prida analyzed the data, participated in the results discussions, and equally contributed to the manuscript preparation. All of the authors revised and accepted the final version of the manuscript.

Conflicts of Interest: The authors declare no conflict of interest.

References

1. Ferry, D.K. Nanowires in Nanoelectronics. *Science* **2008**, *319*, 579–580. [CrossRef] [PubMed]
2. Ferry, D.K.; Gilbert, M.J.; Akis, R. Some Considerations on Nanowires in Nanoelectronics. *IEEE Trans. Electron Devices* **2008**, *55*, 2820–2826. [CrossRef]
3. Zhou, W.; Dai, X.; Fu, T.-M.; Xie, C.; Liu, J.; Lieber, C.M. Long Term Stability of Nanowire Nanoelectronics in Physiological Environments. *Nano Lett.* **2014**, *14*, 1614–1619. [CrossRef] [PubMed]
4. Li, Y.; Qian, F.; Xiang, J.; Lieber, C.M. Nanowire Electronic and Optoelectronic Devices. *Mater. Today* **2006**, *9*, 19–27. [CrossRef]
5. Liu, Q.; Zheng, X.; He, J.; Wang, W.; Fu, M.; Cao, Y.; Li, H.; Wu, Y.; Chen, T.; Zhang, C.; et al. Enhanced Magneto-Optical Effects in Composite Coaxial Nanowires Embedded with Ag Nanoparticles. *Sci. Rep.* **2016**, *6*, 29170. [CrossRef] [PubMed]
6. Valente, J.; Ou, J.-Y.; Plum, E.; Youngs, I.J.; Zheludev, N.I. A Magneto-Electro-Optical Effect in a Plasmonic Nanowire Material. *Nat. Commun.* **2015**, *6*, 7021. [CrossRef] [PubMed]
7. Armelles, G.; Cebollada, A.; García-Martín, A.; Montero-Moreno, J.M.; Waleczek, M.; Nielsch, K. Magneto-optical Properties of Core−Shell Magneto-plasmonic Au-$Co_xFe_{3-x}O_4$ Nanowires. *Langmuir* **2012**, *28*, 9127–9130. [CrossRef] [PubMed]
8. Armelles, G.; Dmitriev, A. Focus on Magnetoplasmonics. *New J. Phys.* **2014**, *16*, 045012. [CrossRef]
9. Gong, S.; Cheng, W. One-dimensional Nanomaterials for Soft Electronics. *Adv. Electron. Mater.* **2016**. [CrossRef]
10. Terris, B.D.; Thomson, T. Nanofabricated and Self-Assembled Magnetic Structures as Data Storage Media. *J. Phys. D Appl. Phys.* **2005**, *38*, R199–R222. [CrossRef]
11. Ai, Y.; Lou, Z.; Li, L.; Chen, S.; Park, H.S.; Wang, Z.M.; Shen, G. Meters-Long Flexible $CoNiO_2$-Nanowires@Carbon-Fibers Based Wire-Supercapacitors for Wearable Electronics. *Adv. Mater. Technol.* **2016**, *1*, 1600142. [CrossRef]

12. Niemann, A.C.; Böhnert, T.; Michel, A.-K.; Bäßler, S.; Gotsmann, B.; Neuróhr, K.; Tóth, B.; Péter, L.; Bakonyi, I.; Vega, V.; et al. Thermoelectric Power Factor Enhancement by Spin-Polarized Currents-A Nanowire Case Study. *Adv. Electron. Mater.* **2016**, *2*, 1600058. [CrossRef]
13. Athanassiou, E.K.; Grossmann, P.; Grass, R.N.; Stark, W.J. Template free, large scale synthesis of cobalt nanowires using magnetic fields for alignment. *Nanotechnology* **2007**, *18*, 165606. [CrossRef]
14. Liu, C.; Li, C.; Ahmed, K.; Mutlu, Z.; Ozkan, C.S.; Ozkan, M. Template Free and Binderless NiO Nanowire Foam for Li-ion Battery Anodes with Long Cycle Life and Ultrahigh Rate Capability. *Sci. Rep.* **2016**, *6*, 29183. [CrossRef] [PubMed]
15. Lopes, M.C.; de Oliveira, C.P.; Pereira, E.C. Computational modeling of the template-assisted deposition of nanowires. *Electrochim. Acta* **2008**, *53*, 4359–4369. [CrossRef]
16. Stępniowski, W.J.; Salerno, M. Fabrication of nanowires and nanotubes by anodic alumina template-assisted electrodeposition. In *Manufacturing Nanostructures*; Ahmed, W., Ali, N., Eds.; One Central Press (OCP): Manchester, UK, 2014; Chapter 12; pp. 321–357.
17. Sousa, C.T.; Leitao, D.C.; Proenca, M.P.; Ventura, J.; Pereira, A.M.; Araujo, J.P. Nanoporous Alumina as Templates for Multifunctional Applications. *Appl. Phys. Rev.* **2014**, *1*, 031102. [CrossRef]
18. Prida, V.M.; Vega, V.; García, J.; Iglesias, L.; Hernando, B.; Minguez-Bacho, I. 1—Electrochemical methods for template-assisted synthesis of nanostructured materials. In *Magnetic Nano- and Microwires: Design, Synthesis, Properties and Applications*; Vazquez, M., Ed.; Woodhead Publishing Series in Electronic and Optical Materials; Elsevier: Amsterdam, The Netherlands, 2015; Chapter 1; pp. 3–39.
19. Da Câmara Santa Clara Gomes, T.; De La Torre Medina, J.; Lemaitre, M.; Piraux, L. Magnetic and Magnetoresistive Properties of 3D Interconnected NiCo Nanowire Networks. *Nanoscale Res. Lett.* **2016**, *11*, 466. [CrossRef] [PubMed]
20. Prida, V.M.; García, J.; Hernando, B.; Bran, C.; Vivas, L.G.; Vázquez, M. 2—Electrochemical synthesis of magnetic nanowires with controlled geometry and magnetic anisotropy. In *Magnetic Nano- and Microwires: Design, Synthesis, Properties and Applications*; Vazquez, M., Ed.; Woodhead Publishing Series in Electronic and Optical Materials; Elsevier: Amsterdam, The Netherlands, 2015; Chapter 2; pp. 41–104.
21. García, J.; Prida, V.M.; Vivas, L.G.; Hernando, B.; Barriga-Castro, E.D.; Mendoza-Reséndez, R.; Luna, C.; Escrig, J.; Vázquez, M. Magnetization reversal dependence on effective magnetic anisotropy in electroplated Co–Cu nanowire arrays. *J. Mater. Chem. C* **2015**, *3*, 4688–4697. [CrossRef]
22. Prida, V.M.; García, J.; Iglesias, L.; Vega, V.; Görlitz, D.; Nielsch, K.; Barriga-Castro, E.D.; Mendoza-Reséndez, R.; Ponce, A.; Luna, C. Electroplating and Magnetostructural Characterization of Multisegmented $Co_{54}Ni_{46}/Co_{85}Ni_{15}$ Nanowires From Single Electrochemical Bath in Anodic Alumina Templates. *Nanoscale Res. Lett.* **2013**, *8*, 263. [CrossRef] [PubMed]
23. Jang, B.; Pellicer, E.; Guerrero, M.; Chen, X.; Choi, H.; Nelson, B.J.; Sort, J.; Pané, S. Fabrication of Segmented Au/Co/Au Nanowires: Insights in the Quality of Co/Au Junctions. *ACS Appl. Mater. Interfaces* **2014**, *6*, 14583–14589. [CrossRef] [PubMed]
24. Ivanov, Y.P.; Chuvilin, A.; Lopatin, S.; Kosel, J. Modulated Magnetic Nanowires for Controlling Domain Wall Motion: Toward 3D Magnetic Memories. *ACS Nano* **2016**, *10*, 5326–5332. [CrossRef] [PubMed]
25. Minguez-Bacho, I.; Rodriguez-López, S.; Vázquez, M.; Hernández-Vélez, M.; Nielsch, K. Electrochemical synthesis and magnetic characterization of periodically modulated Co nanowires. *Nanotechnology* **2014**, *25*, 145301. [CrossRef] [PubMed]
26. Iglesias-Freire, O.; Bran, C.; Berganza, E.; Mínguez-Bacho, I.; Magén, C.; Vázquez, M.; Asenjo, A. Spin configuration in isolated FeCoCu nanowires modulated in diameter. *Nanotechnology* **2015**, *26*, 395702. [CrossRef] [PubMed]
27. Bran, C.; Berganza, E.; Palmero, E.M.; Fernandez-Roldan, J.A.; Del Real, R.P.; Aballe, L.; Foerster, M.; Asenjo, A.; Rodríguez, A.F.; Vazquez, M. Spin configuration of cylindrical bamboo-like magnetic nanowires. *J. Mater. Chem. C* **2016**, *4*, 978–984. [CrossRef]
28. Berganza, E.; Bran, C.; Vazquez, M.; Asenjo, A. Domain wall pinning in FeCoCu bamboo-like nanowires. *Sci. Rep.* **2016**, *6*, 29702. [CrossRef] [PubMed]
29. Rodríguez, L.A.; Bran, C.; Reyes, D.; Berganza, E.; Vázquez, M.; Gatel, C.; Snoeck, E.; Asenjo, A. Quantitative Nanoscale Magnetic Study of Isolated Diameter-Modulated FeCoCu Nanowires. *ACS Nano* **2016**, *10*, 9669–9678. [CrossRef] [PubMed]

30. Montazer, A.H.; Ramazani, A.; Kashiab, M.A.; Zavašnikc, J. Angular-dependent magnetism in Co(001) single-crystal nanowires: Capturing the vortex nucleation fields. *J. Mater. Chem. C* **2016**, *4*, 10664–10674. [CrossRef]
31. Zhang, J.; Pané, S.; Sort, J.; Pellicer, E. Toward Robust Segmented Nanowires: Understanding the Impact of Crystallographic Texture on the Quality of Segment Interfaces in Magnetic Metallic Nanowires. *Adv. Mater. Interfaces* **2016**, *3*, 1600336. [CrossRef]
32. Agramunt-Puig, S.; Del-Valle, N.; Pellicer, E.; Zhang, J.; Nogués, J.; Navau, C.; Sanchez, A.; Sort, J. Modeling the collective magnetic behavior of highly-packed arrays of multi-segmented nanowires. *New J. Phys.* **2016**, *18*, 013026. [CrossRef]
33. Geng, X.; Podlaha, E.J. Coupled, Simultaneous Displacement and Dealloying Reactions into Fe–Ni–Co Nanowires for Thinning Nanowire Segments. *Nano Lett.* **2016**, *16*, 7439–7445. [CrossRef] [PubMed]
34. Reyes, D.; Biziere, N.; Warot-Fonrose, B.; Wade, T.; Gatel, C. Magnetic Configurations in Co/Cu Multilayered Nanowires: Evidence of Structural and Magnetic Interplay. *Nano Lett.* **2016**, *16*, 1230–1236. [CrossRef] [PubMed]
35. Özkale, B.; Shamsudhin, N.; Chatzipirpiridis, G.; Hoop, M.; Gramm, F.; Chen, X.; Martí, X.; Sort, J.; Pellicer, E.; Pané, S. Multisegmented FeCo/Cu Nanowires: Electrosynthesis, Characterization, and Magnetic Control of Biomolecule Desorption. *ACS Appl. Mater. Interfaces* **2015**, *7*, 7389–7396. [CrossRef] [PubMed]
36. Zhang, J.; Agramunt-Puig, S.; Del-Valle, N.; Navau, C.; Baró, M.D.; Estradé, S.; Peiró, F.; Pané, S.; Nelson, B.J.; Sanchez, A.; et al. Tailoring Staircase-like Hysteresis Loops in Electrodeposited Trisegmented Magnetic Nanowires: A Strategy toward Minimization of Interwire Interactions. *ACS Appl. Mater. Interfaces* **2016**, *8*, 4109–4117. [CrossRef] [PubMed]
37. Ramulu, T.S.; Venu, R.; Sinha, B.; Yoon, S.S.; Kim, C.G. Electrodeposition of CoPtP/Au Multisegment Nanowires: Synthesis and DNA Functionalization. *Int. J. Electrochem. Sci.* **2012**, *7*, 7762–7769.
38. Masuda, H.; Fukuda, K. Ordered metal nanohole arrays made by s two-step replication of honeycomb structures of anodic alumina. *Science* **1995**, *268*, 1466–1468. [CrossRef] [PubMed]
39. Prida, V.M.; Pirota, K.R.; Navas, D.; Asenjo, A.; Hernández-Vélez, M.; Vázquez, M. Self-Organized Magnetic Nanowire Arrays Based on Alumina and Titania Templates. *J. Nanosci. Nanotechnol.* **2007**, *7*, 272–285. [PubMed]
40. Romero, V.; Vega, V.; García, J.; Zierold, R.; Nielsch, K.; Prida, V.M.; Hernando, B.; Benavente, J. Changes in Morphology and Ionic Transport Induced by ALD SiO_2 Coating of Nanoporous Alumina Membranes. *ACS Appl. Mater. Interfaces* **2013**, *5*, 3556–3564. [CrossRef] [PubMed]
41. Bachmann, J.; Zierold, R.; Chong, Y.T.; Hauert, R.; Sturm, C.; Schmidt-Grund, R.; Rheinlander, B.; Grundmann, M.; Gosele, U.; Nielsch, K. A Practical, Self-Catalytic, Atomic Layer Deposition of Silicon Dioxide. *Angew. Chem.* **2008**, *47*, 6177–6179. [CrossRef] [PubMed]
42. Vega, V.; Böhnert, T.; Martens, S.; Waleczek, M.; Montero-Moreno, J.M.; Görlitz, D.; Prida, V.M.; Nielsch, K. Tuning the Magnetic Anisotropy of Co-Ni Nanowires: Comparison Between Single Nanowires and Nanowire Arrays in Hard-Anodic Aluminum Oxide Membranes. *Nanotechnology* **2012**, *23*, 465709. [CrossRef] [PubMed]
43. Materials Analysis Using Diffraction. Available online: http://maud.radiographema.com (accessed on 26 February 2017).
44. Lutterotti, L. Total pattern fitting for the combined size-strain-stress-texture determination in thin film diffraction. *Nuclear Instrum. Methods Phys. Res. B* **2010**, *268*, 334–340. [CrossRef]
45. Lutterotti, L.; Bortolotti, M.; Ischia, G.; Lonardelli, I.; Wenk, H.-R. Rietveld texture analysis from diffraction images. *Z. Kristallogr.* **2007**, *Suppl. 26*, 125–130. [CrossRef]
46. Lutterotti, L.; Chateigner, D.; Ferrari, S.; Ricote, J. Texture, Residual Stress and Structural Analysis of Thin Films using a Combined X-Ray Analysis. *Thin Solid Films* **2004**, *450*, 34–41. [CrossRef]
47. García, J.; Vega, V.; Iglesias, L.; Prida, V.M.; Hernando, B.; Barriga-Castro, E.D.; Mendoza-Reséndez, R.; Luna, C.; Görlitz, D.; Nielsch, K. Template-assisted Co-Ni Alloys and Multisegmented Nanowires with Tuned Magnetic Anisotropy. *Phys. Status Solidi A* **2014**, *211*, 1041–1047. [CrossRef]
48. Hertel, R. Micromagnetic simulations of magnetostatically coupled Nickel nanowires. *J. Appl. Phys.* **2001**, *90*, 5752–5758. [CrossRef]
49. Zighem, F.; Maurer, T.; Ott, F.; Chaboussant, G. Dipolar interactions in arrays of ferromagnetic nanowires: A micromagnetic study. *J. Appl. Phys.* **2011**, *109*, 013910. [CrossRef]

50. Vega, V.; Prida, V.M.; García, J.A.; Vázquez, M. Torque magnetometry analysis of magnetic anisotropy distribution in Ni nanowire arrays. *Phys. Stat. Solidi A* **2011**, *208*, 553–558. [CrossRef]
51. Salem, M.S.; Sergelius, P.; Corona, R.M.; Escrig, J.; Görlitz, D.; Nielsch, K. Magnetic properties of cylindrical diameter modulated $Ni_{80}Fe_{20}$ nanowires: Interaction and coercive fields. *Nanoscale* **2013**, *5*, 3941–3947. [CrossRef] [PubMed]
52. Raposo, V.; Zazo, M.; Flores, A.G.; García, J.; Vega, V.; Iñiguez, J.; Prida, V.M. Ferromagnetic resonance in low interacting permalloy nanowire arrays. *J. Appl. Phys.* **2016**, *114*, 143903. [CrossRef]
53. Barandiaran, J.M.; Vázquez, M.; Hernando, A.; González, J.; Rivero, G. Distribution of the Magnetic Anisotropy in Amorphous Alloys Ribbons. *IEEE Trans. Magn.* **1989**, *25*, 3330–3332. [CrossRef]
54. De la Torre Medina, J.; Darques, M.; Piraux, L.; Encinas, A. Application of the anisotropy field distribution method to arrays of magnetic nanowires. *J. Appl. Phys.* **2009**, *105*, 023909. [CrossRef]